# Purification of Gold Nanoplates Grown Directly on Surfaces for Enhanced Localized Surface Plasmon Resonance Biosensing

**Srinivas R. Beeram and Francis P. Zamborini***

Department of Chemistry, University of Louisville, Louisville, Kentucky 40292

**ABSTRACT** Here we describe the synthesis and purification of Au nanoplates grown directly on surfaces by a chemical seed-mediated growth method. The synthesis involves the attachment of 3−5 nm diameter Au nanoparticle (NP) seeds onto glass and Si/$SiO_x$ surfaces and their subsequent growth into larger Au nanostructures by the chemical reduction of $AuCl_4^-$ with ascorbic acid in the presence of cetyltrimethylammonium bromide (CTAB). We used two different growth solutions. Growth solution 1 (GS1) led to a sample with 74% Au nanospheres and 26% Au nanoplates, while growth solution 2 (GS2), with lower CTAB and higher ascorbic acid concentration, led to 56% nanospheres and 44% nanoplates. The average wavelength of maximum extinction ($\lambda_{max}$) of the localized surface plasmon resonance (LSPR) band of these samples was 549 and 627 nm, respectively. The use of adhesive tape or sonication enables the preferential removal of spherical Au nanostructures in both cases, leaving samples with >90% Au nanoplates. The average $\lambda_{max}$ increased to 672 nm (GS1) and 664 nm (GS2) for taped samples and 780 nm (GS1) and 720 nm (GS2) for sonicated samples, consistent with a higher purity of Au nanoplates on the surface. In all cases, the purified nanoplates vary in size and shape, including triangular, circular, or hexagonal structures, leading to broad spectra or the appearance of multiple peaks. We tuned the average $\lambda_{max}$ of the LSPR band of the Au nanoplate samples from 540 to 780 nm by varying the sonication time from 0 to 135 s. The change in $\lambda_{max}$ upon binding of anti-IgG to the edges of the purified nanoplates increases with an increasing number of anti-IgG on the edges, is 4−8 times larger compared to that of spherical nanoparticles, and is larger for samples purified by sonication compared to taping because the former has a larger initial $\lambda_{max}$. A sample of Au nanoplates purified by taping and functionalized with anti-IgG at the edge sites displayed a shift in $\lambda_{max}$ as large as 45 nm for a 10 pg/mL solution of IgG (<1 pM).

**KEYWORDS:** localized surface plasmon resonance (LSPR) · gold · nanoplates · AFM · biosensing · immunoassay · nanoparticles · plasmonics · spectroscopy

The conduction band electrons of metal nanoparticles collectively oscillate upon interaction with electromagnetic radiation of an appropriate frequency. These oscillations are known as localized surface plasmons, and this phenomenon is the basis of localized surface plasmon resonance spectroscopy (LSPR).[1,2] For some noble metals, especially Au and Ag, the frequency of these collective oscillations matches that of visible or near-infrared light, leading to a strong absorbance or scattering in that region. The particular wavelength of maximum extinction ($\lambda_{max}$) is well-known to depend on the composition, size, and shape of the nanostructure as well as the refractive index of the surrounding environment.[1,2] Accordingly, many researchers have exploited the optical properties of metal nanostructures for chemical and biosensing applications. The detection of a molecular analyte of interest is possible by functionalizing a metal nanostructure with an appropriate receptor, which leads to selective binding of the molecular analyte and, if a local change in the refractive index occurs, a shift in $\lambda_{max}$ of the LSPR band. This strategy has been used previously to detect proteins,[3−9] DNA,[10−12] vapor molecules,[13] polymers,[14] and metal ions.[15,16] The magnitude of the shift in $\lambda_{max}$ depends on the number of bound analyte molecules, their distance from the metal nanostructure, the difference between the refractive index of the analyte and the global environment, the size of the analyte, the bulk refractive index sensitivity of the nanostructure, and the location of the binding analyte.[17]

Our group has been interested in controlling and directly measuring the binding location of proteins on metal nanostructures and correlating that with the change in $\lambda_{max}$ in the LSPR spectrum. We recently reported on the controlled attachment of human anti-IgG to the edge and vertex sites of Au nanostructures.[18] In that work, we synthesized Au nanostructures directly on surfaces that were ~77% Au nanospheres and ~23% Au nanoplates. The optical data showed that preferential binding of anti-IgG to the edge and vertex sites of these nanostructures led to dramatically higher changes in $\lambda_{max}$ compared to random binding on terrace sites. For the first time, we

*Address correspondence to f.zamborini@louisville.edu.

Received for review October 28, 2009 and accepted June 11, 2010.

**Published online June 24, 2010.**
10.1021/nn1007397

correlated the LSPR spectra with atomic force microscopy (AFM) images that confirmed the location of binding (edges, vertices, or terraces). The main drawback of this work was that we correlated the binding location obtained from AFM images of smooth Au nanoplates with LSPR spectra dominated by the 77% Au nanospheres. While we concluded that the binding location on the Au nanoplates reflected the binding location on Au nanospheres, we still lack a direct correlation between protein binding location and the LSPR spectrum on Au nanoplates. Accordingly, our goal in this work was to synthesize samples of nearly pure Au nanoplates.

Au nanoplates are the ideal metal nanostructure for determining the effect of binding location on the shift in $\lambda_{max}$ of the LSPR spectrum because they (1) are atomically smooth, which allows easy visualization of molecules attached to the surface by AFM, and (2) have different sites with different LSPR properties. We already demonstrated imaging the location of human anti-IgG bound directly on Au nanoplates, and others have shown by theoretical calculations[19] and electron energy loss spectroscopy (EELS)[20] that the electromagnetic field strength of the localized surface plasmons increases in the order of vertex sites > edge sites > terrace sites of metal nanoplates. The energy of the surface plasmons depends on the exact size and shape of the nanoplate but generally follows the order vertex < edge < terrace.[20] There have been some qualitative studies showing location-dependent shifts in $\lambda_{max}$ upon analyte binding to metal nanostructures[3,10] but none directly correlating the location of the bound analyte with the LSPR spectrum of the same sample on nanoplates or other structures. In this article, we describe two new methods for the synthesis and purification of Au nanoplates directly on surfaces that allowed us to measure the shift in the LSPR $\lambda_{max}$ upon human anti-IgG binding and correlate it to AFM images showing the anti-IgG coverage and binding location.

Several methods exist for synthesizing Au and Ag metal nanoplates in solution or directly on surfaces. Solution-based methods for synthesizing Au nanoplates include chemical, electrochemical,[21] and photochemical[22,23] reduction of a Au complex (usually $AuCl_4^-$) in the presence of a stabilizer. Some common chemical reducing agents include ethylene glycol,[24−26] a polyamine,[27,28] lemongrass extract of a plant,[29] polyvinylpyrrolidone (PVP),[30] ascorbic acid,[31] tartaric acid,[22] sodium citrate,[32−34] salicylic acid,[35] natural humic substance,[36] and formaldehyde[37] in the presence of stabilizers, such as cetyltrimethylammonium bromide (CTAB), cetyltrimethylammonium chloride (CTACl), PVP, or ionic liquids. The chemical reduction often involved heating,[22,24−26,28,30,32−36] and in some cases, the reducing agent and stabilizer are the same.[28,30,36,38] Au nanoplates have also been synthesized within PVA polymer films[38] where PVA is also the stabilizer, in ionic liquids[39] with heating, and in liquid crystals made of block copolymers[40] at room temperature. Photochemical methods used CTACl and PVA as stabilizing agents,[22,23] and in one case, laser ablation of solid Au metal in solution led to Au nanoplates.[41] Solution-based chemical methods for synthesizing Ag metal nanoplates involve the laser ablation of Ag metal[41] or chemical reduction of $Ag^+$ by PVP[30,42] and dimethylformamide[43] through heating in the presence of a stabilizer. Light[44−48] and heat[49] induced conversion of nanospheres to nanoplates, and heat[50] and light[51−53] induced shape changes of nanoplates have also been reported. Several groups have reported the chemical seed-mediated synthesis of Au and Ag nanoplates in solutions.[54−60] High yields of Ag nanoplates (>95%)[54] and Au nanoplates (96%)[26] in solution have been reported both with[59] and without[26,54] purification. The main disadvantage of the synthesis of nanoplates in solution is that they need to later be assembled on a surface for various sensor or other plasmonic-based applications. The large excess of surfactant or polymer usually present can often make the assembly of well-isolated nanoplates on surfaces a challenge. Han and co-workers recently assembled Ag nanoprisms by two different methods on a surface from solution and observed their different optical properties,[61] but this has not yet been reported for Au nanoplates.

There are examples of synthesizing Au and Ag nanoplates directly on a surface.[18,62−67] Van Duyne and co-workers pioneered the use of nanosphere lithography (NSL), a method to fabricate well-ordered arrays of Ag, Cu, and Al nanoplates directly on surfaces by vapor deposition of the metal of interest through an ordered array of polymeric spheres acting as a mask.[67−69] Our group and others previously reported on the use of seed-mediated growth of Au or Ag nanoplates directly on surfaces.[18,62,63,65,66] The general synthesis involves deposition of seed onto the surface and growth of these nanoparticle seeds into nanoplates by the reduction of metal salt in the presence of a stabilizer (CTAB or PVP). Geddes and co-workers reported an 80% yield for Ag nanoplates,[62] and others reported a 30−60% yield for Au nanoplates.[65,66] Sun *et al.* reported a high-yield, size-controlled synthesis of Ag nanoplates by galvanic exchange directly on an n-type semiconductor substrate.[64] Nanoplates have been utilized in various applications, including catalysis,[70−72] surface-enhanced Raman spectroscopy (SERS),[36] and LSPR-based biosensing.[3]

Here we describe the seed-mediated synthesis of Au nanoplates directly on glass and $Si/SiO_x$ surfaces using two different methods with yields ranging from 26 to 44%, where the majority of the surface contains spherical Au nanoparticles. Importantly, we report the use of adhesive tape and sonication to selectively remove the spherical nanoparticles, resulting in surfaces with >90% Au nanoplates. This method is beneficial

over NSL in that it is an all-chemical benchtop approach that does not require as many steps or high vacuum metal evaporation systems. Although NSL leads to highly uniform structures on the surface, the nanoplates synthesized by our method are well-isolated from one another and highly crystalline. Our purification strategy leads to a higher yield of nanoplates on the surface when compared to other seed-mediated growth methods directly on surfaces. While it may be possible to synthesize Au nanoplates in solution in high yield and assemble them onto surfaces, we have not found any literature examples and believe our method will be better for assembling well-isolated nanoplates on surfaces with no aggregation. To demonstrate the significance of our synthesis and purification strategy for biosensing, we attached human anti-IgG to the edge and vertex sites of the purified Au nanoplates and correlated the change in $\lambda_{max}$ with the binding location and coverage as determined by AFM. Finally, we show that the $\lambda_{max}$ of purified Au nanoplates on glass functionalized with human anti-IgG selectively on edge and vertex sites is highly sensitive to $<1$ pM IgG (10 pg/mL). Our simple benchtop chemical synthesis, functionalization, and purification method leads to highly sensitive devices for optical-based protein detection that may find use in future biomedical applications.

## RESULTS AND DISCUSSION

**Synthesis of Au Nanoplates Directly on Surfaces.** We synthesized Au nanostructures directly on glass and Si/$SiO_x$ surfaces using a similar seed-mediated growth procedure described by our group previously,[73−77] which is based on the solution seed-mediated synthesis of Au nanorods described by Murphy and co-workers.[78] In our procedure, we deposited 4 nm average diameter Au "seed" nanoparticles onto thiol-functionalized glass or Si/$SiO_x$ substrates and then grew these seeds into larger nanostructures by electroless reduction of $AuCl_4^-$ onto the seeds with ascorbic acid in the presence of cetyltrimethylammonium bromide (CTAB). Figure 1A,B shows scanning electron microscopy (SEM) images of Si/$SiO_x$ substrates prepared in this way using two different growth solutions. We grew the Au nanostructures in Figure 1A in growth solution 1 (GS1), which contained 9 mL of 0.10 M CTAB, 450 μL of 0.01 M $HAuCl_4$, and 50 μL of 0.1 M ascorbic acid, and grew those in Figure 1B in growth solution 2 (GS2), which contained 9 mL of 0.016 M CTAB, 450 μL of 0.01 M $HAuCl_4$, and 150 μL of 0.2 M ascorbic acid.

The bright features in the images correspond to individual or small aggregates of spherical Au nanoparticles, and the darker circular, hexagonal, or triangular structures are Au nanoplates, as indicated in the images. We define the Au nanoplates as structures with an aspect ratio greater than 2, with the aspect ratio defined as the width of the nanoplate divided by the height. We determined the average width, height, and aspect ratio of the nanoplates using AFM or a combination of SEM (for width measurement) and AFM (for height measurement). The average width, height, and aspect ratio were 203 ± 50 nm, 37 ± 12 nm, and 6.1 ± 2.5, respectively, based on AFM images and 163 ± 46 nm, 37 ± 12 nm, and 4.4 ± 1.9, respectively, based on combined SEM and AFM images for nanoplates synthesized by GS1. These values were 214 ± 46 nm, 31 ± 5 nm, and 7.1 ± 2.1, respectively, based on AFM and 184 ± 43 nm, 31 ± 5 nm, and 5.9 ± 1.7, respectively, based on AFM and SEM for nanoplates synthesized by GS2.

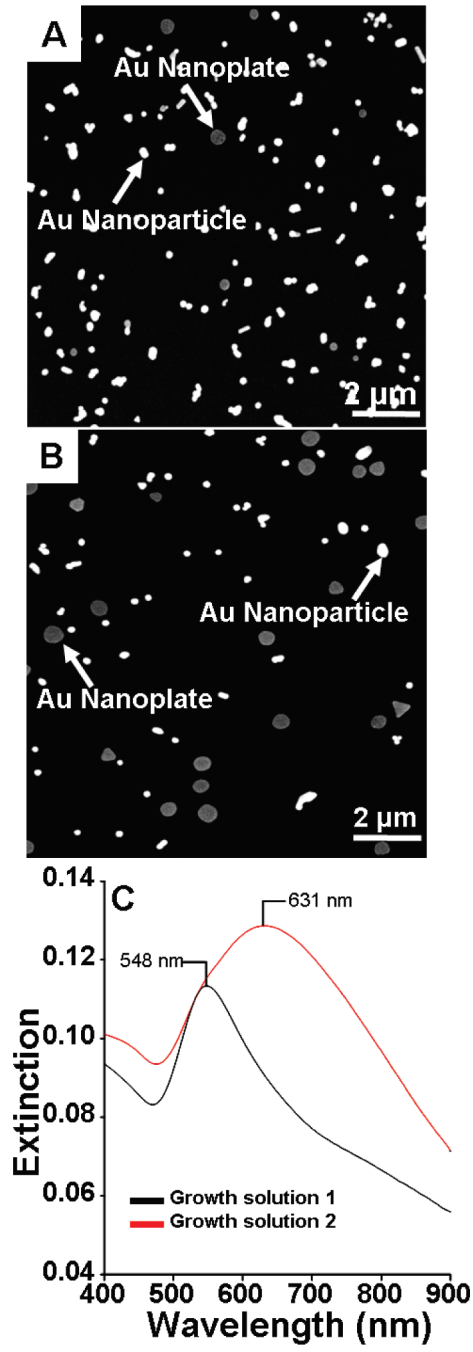


**Figure 1. Scanning electron microscopy (SEM) images of Au nanostructures grown directly on Si/$SiO_x$ by (A) growth solution 1 and (B) growth solution 2. (C) LSPR spectra of Au nanostructures grown on glass with growth solutions 1 and 2.**

The nanoplates synthesized by GS2 have a higher aspect ratio compared to those synthesized by GS1, and the aspect ratio is smaller in both cases based on the SEM measurements due to the smaller average width values, which is likely due to an exaggerated width in the AFM images due to the radius of curvature of the AFM tip. Table S1 of the Supporting Information shows all of the statistics of the dimensions and aspect ratio of the Au nanoplates.

The yields of Au nanoplates were 26 and 44% for samples prepared with GS1 and GS2, respectively. The amount of $AuCl_4^-$ was equal in both growth solutions, but the CTAB concentration was lower by a factor of ~6, and the ascorbic acid concentration was larger by a factor of 6 in GS2. It is not clear at this time why this particular change in growth solution led to a larger yield of Au nanoplates. We previously used GS1 with a different source of CTAB for growing Au nanorods directly on surfaces.[73−77] With this particular CTAB source, we found a large yield of Au nanoplates on the surface. Others have recently shown that the type of Au nanostructures grown by seed-mediated growth in the presence of CTAB is sensitive to the source of CTAB (see Methods for more details).[79] Understanding the role of the CTAB source is an important issue but not the focus of this study. Our focus was to demonstrate a method for purifying the Au nanoplates for localized surface plasmon resonance (LSPR) sensing applications.

Figure 1C shows the resulting LSPR spectrum of the Au nanostructures synthesized on a glass sample using GS1 and GS2 in the seed-mediated growth method. The spectra of the Au nanostructures show an extinction maximum at about 548 nm (black) and at 631 nm (red) for those prepared using GS1 and GS2, respectively. The maximum of 548 nm is the expected position of spherical Au nanoparticles,[18] which is the dominant product (74%) in the synthesis with GS1. As the amount of Au nanoplates increased relative to the Au spherical nanoparticles using GS2 (56% spheres), the extinction maxima red-shifted to 631 nm, which is consistent with the extinction maxima of Au nanoplates reported in the literature (600−2000 nm, depending on the dimensions).[29,32]

**Purification of Au Nanoplates by Taping.** While the percentage of Au nanoplates is larger using GS2 compared to GS1, both conditions led to samples with a majority of spherical Au nanoparticles. It has been well-established that the LSPR extinction maxima ($\lambda_{max}$) of nanoplates is more sensitive to refractive index changes[80,81] of the environment and to biomolecular binding events[80,81] compared to that of Au nanospheres, making it crucial to develop simple benchtop synthesis strategies for preparing substrates with a high percentage of Au nanoplates on the surface. On the basis of our previous success with the purification of Au and Ag nanorods (NRs),[75,82] we applied Scotch tape adhesive to the surface and slowly removed the tape in order to selectively remove the spherical nanoparticles. Figure 2A,B shows atomic force microscopy (AFM) images of $Si/SiO_x$ substrates after the synthesis of Au nanostructures using GS1 and GS2, respectively, and removal of spherical nanoparticles using the tape method. It is clear that the tape removed most of the spherical nanoparticles when comparing these images to the SEM images in Figure 1A,B. These samples contained 90 ± 11 and 89 ± 7% Au nanoplates for those prepared by GS1 and GS2, respectively, based on AFM images of at least four regions of three samples. The purified samples contained mostly Au nanoplates, although there remained a large dispersity in the particular size and shape of the nanoplate (triangular, hexagonal, circular, *etc.*). The average height, width, and aspect ratio of the Au nanoplates were 183 ± 41 nm, 29 ± 5 nm, and 6.4 ± 2.1 for those synthesized by GS1 and 216 ± 45 nm, 32 ± 10 nm, and 7.5 ± 2.8 for those synthesized by GS2, based on AFM images. These values were 153 ± 33 nm, 29 ± 5 nm, and 5.3 ± 1.4 for those synthesized by GS1 and 179 ± 34 nm, 32 ± 10 nm, and 5.6 ± 2.1 for those synthesized by GS2, based on SEM and AFM images. The average aspect ratio was similar for both synthesis methods after taping and similar to the average aspect ratio before taping in both cases based on combined SEM and AFM images.

Figure 2C,D shows the LSPR spectra before and after the taping of Au nanostructures on glass samples synthesized using GS1 and GS2, respectively. In both cases, the LSPR spectrum before taping was similar to that shown in Figure 1C, where the extinction maxima were 558 and 625 nm for GS1 and GS2, respectively. After taping, the extinction at all wavelengths decreased and the $\lambda_{max}$ of the LSPR band red-shifted for both samples. The $\lambda_{max}$ shifted from 558 to 672 nm and from 625 to 689 nm for the Au nanostructures synthesized with GS1 and GS2, respectively. Figure 2E,F shows expanded plots of the LSPR spectra after taping. The loss in extinction after taping was due to the removal of the spherical Au nanoparticles and likely a few nanoplates. The shift in $\lambda_{max}$ occurred because the Au nanoplates, which now dominate the surface, exhibit a LSPR band between 600 and 2000 nm, depending on their exact shape, thickness, and edge length.[32] The peaks at 672 and 689 nm are consistent with the measured average aspect ratio of the nanoplates. The bands are fairly broad in Figure 2E,F, extending from 500 to 900 nm, which we believe is mainly due to the size and shape dispersity of the nanoplates. The main difference between the samples synthesized by GS1 and GS2 is that the latter had a broader spectrum and larger extinction value. The larger extinction value is consistent with the larger percentage of nanoplates on the surface prior to taping (44 *versus* 26%), and the broader spectrum is likely due to a larger dispersity in nanoplate size and shape. For example, on the basis of SEM and AFM images, the deviation in aspect ratio was 38% for those

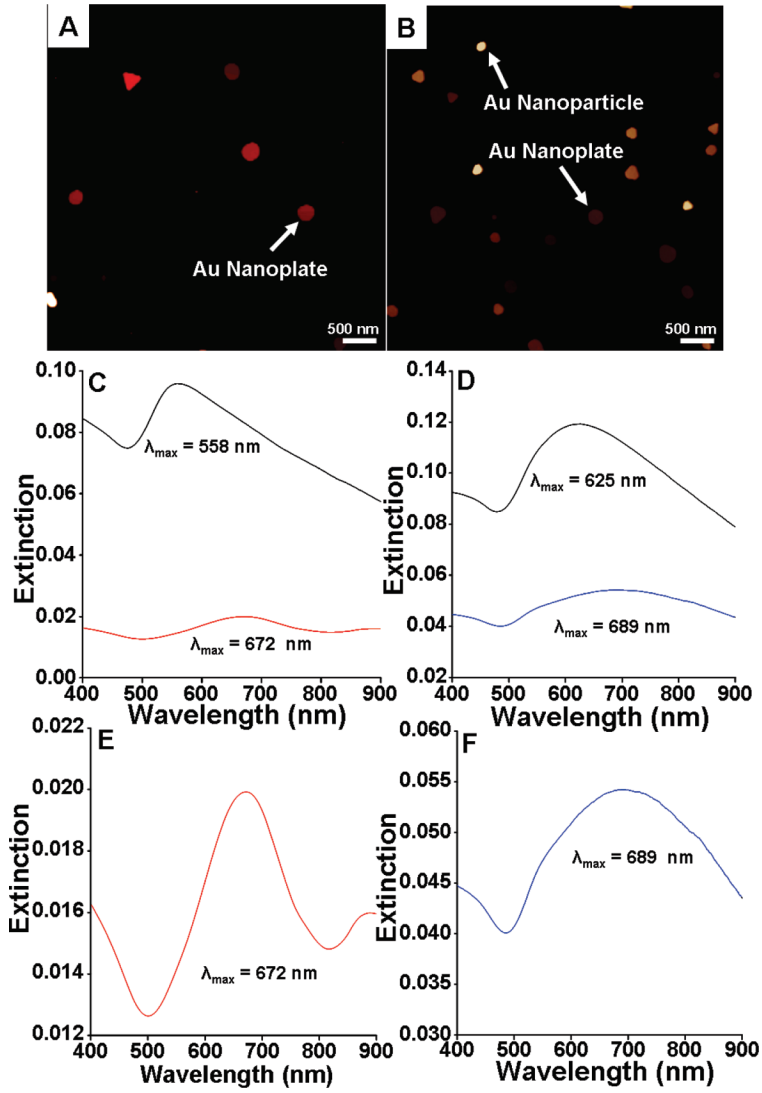


**Figure 2. Atomic force micoscopy (AFM) images of Au nanoplates purified by taping after growth on Si/$SiO_x$ using (A) growth solution 1 and (B) growth solution 2. (C,D) Corresponding LSPR spectra of samples grown on glass by growth solutions 1 and 2, respectively, before (black spectrum) and after (red or blue spectrum) taping. (E,F) Expanded plots after taping in (C) and (D), respectively.**

synthesized by GS2 compared to 26% for those synthesized by GS1 (Table S1, Supporting Information). While the $\lambda_{max}$ was 67 nm more red-shifted for the sample synthesized using GS2 compared to GS1 prior to taping, after taping, the $\lambda_{max}$ value was similar (difference of 17 nm), consistent with a high purity of Au nanoplates for both samples.

**Purification of Au Nanoplates by Sonication.** We also purified samples of Au nanostructures by subjecting the glass or Si/$SiO_x$ slides to sonication. Figure 3A,B shows AFM images of Si/$SiO_x$ substrates after the synthesis of Au nanostructures using GS1 and GS2, respectively, and removal of spherical nanoparticles by sonication in water. As with the tape method, it is clear that sonication removed most of the spherical nanoparticles when comparing these images to the SEM images in Figure 1. These samples contained 91 $\pm$ 9 and 90 $\pm$ 8% Au nanoplates for those prepared by GS1 and GS2, respectively, based on AFM images of at least five regions of three samples. The average height, width, and aspect ratio of the Au nanoplates were 269 $\pm$ 54 nm, 28 $\pm$ 6 nm, and 9.7 $\pm$ 2.6 for those synthesized by GS1 and 202 $\pm$ 54 nm, 27 $\pm$ 8 nm, and 8.1 $\pm$ 2.7 for those synthesized by GS2, based on AFM images. These values were 182 $\pm$ 49 nm, 28 $\pm$ 6 nm, and 6.5 $\pm$ 2.3 for those synthesized by GS1 and 187 $\pm$ 48 nm, 27 $\pm$ 8 nm, and 6.9 $\pm$ 2.6 for those synthesized by GS2, based on SEM and AFM images. The average aspect ratio was slightly larger for the samples synthesized by GS1 compared to GS2 after sonication based on the AFM images but similar for both methods based on the combined SEM and AFM images.

Figure 3C,D shows the LSPR spectra before and after sonication of Au nanostructures on glass samples synthesized using GS1 and GS2, respectively. In both cases, the LSPR spectrum before sonication was again similar to that shown in Figure 1C and Figure 2, where the extinction maxima were 548 and 617 nm for GS1

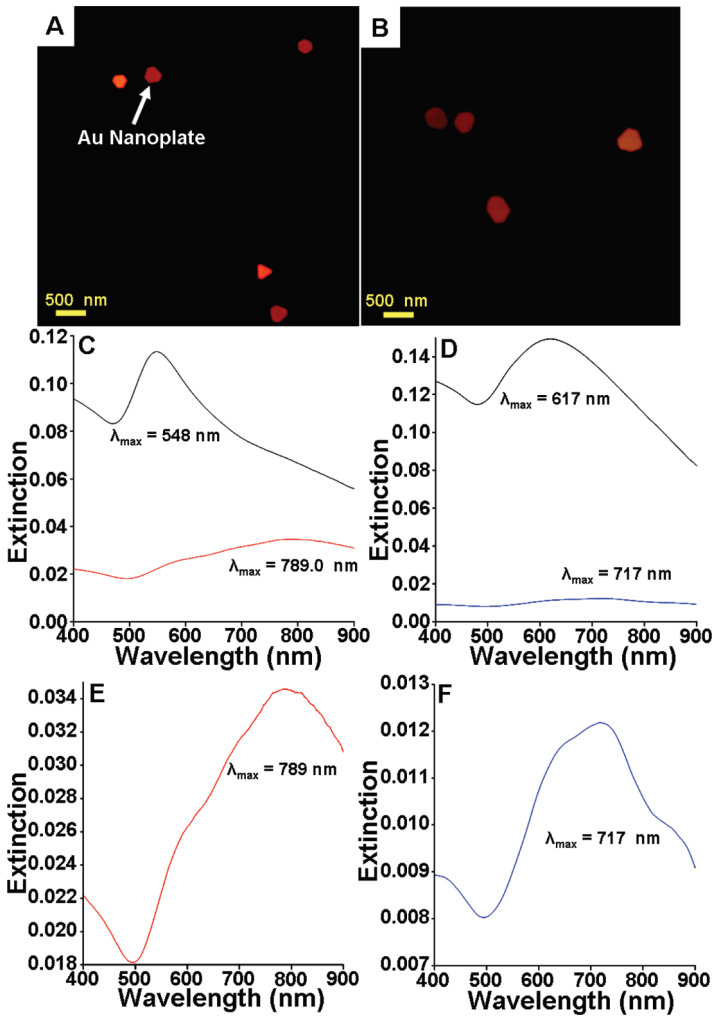


**Figure 3. Atomic force microscopy (AFM) images of Au nanoplates purified by sonication after growth on Si/$SiO_x$ using (A) growth solution 1 and (B) growth solution 2. (C,D) Corresponding LSPR spectra of samples grown on glass by growth solutions 1 and 2, respectively, before (black spectrum) and after (red or blue spectrum) sonication. (E,F) Expanded plots after sonication in (C) and (D), respectively.**

and GS2, respectively. After sonication, the extinction at all wavelengths decreased and the $\lambda_{max}$ of the LSPR band red-shifted to 789 and 717 nm for the Au nanostructures synthesized with GS1 and GS2, respectively, consistent with their measured average aspect ratios. Figure 3E,F shows expanded plots of the LSPR spectra after sonication. Similar to taped samples, the extinction decreased and $\lambda_{max}$ red-shifted significantly, indicative of a sample with a high percentage of nanoplates. The bands were fairly broad, often displaying multiple peaks due to the size and shape dispersity of the nanoplates. The sample shown in Figure 3E, for example, displayed a main LSPR peak at 789 nm, but there were also two shoulder peaks at about 600 and 700 nm. The LSPR spectrum of the sample shown in Figure 3F displayed a main peak at 717 nm and two shoulders at 640 and 850 nm that are likely due to other nanoplate populations present on the substrate. See Figure S1 of Supporting Information for examples of other sonicated samples with multiple peaks in their LSPR spectrum.

We synthesized several samples using GS1 and GS2 and purified them by taping or sonication. Table 1 shows the average $\lambda_{max}$ values and standard deviation of the major peak from all of the samples prepared ($n$ = 3−7 samples). The average $\lambda_{max}$ followed the order of GS1 (549 ± 6 nm) < GS2 (627 ± 13 nm) < GS2 taped (664 ± 23 nm) ≈ GS1 taped (672 ± 15 nm) < GS2 sonicated (720 ± 12 nm) < GS1 sonicated (780 ± 47 nm). The taped samples synthesized by GS1 and GS2 are statistically the same, and the $\lambda_{max}$ is less than the sonicated samples. The GS1 sonicated sample has a slightly larger $\lambda_{max}$ value compared to that of the GS2 sonicated sample.

Table 1 provides the average extinction at $\lambda_{max}$ with standard deviation for samples synthesized by GS1 and GS2 and taped or sonicated. As expected and discussed earlier, the average extinction of the taped GS2 sample was ~3 times larger compared to the taped GS1 sample (0.068 ± 0.014 *versus* 0.027 ± 0.022). This was due to the higher percentage of nanoplates on the GS2 sample before taping compared to the GS1 sample (44 *versus* 26%). In contrast, the extinction value of the GS1 sample was larger compared to GS2 after sonication (0.024 ± 0.008 *versus* 0.011 ± 0.005). This shows that sonication removed many of the Au nanoplates from the surface in addition to the spherical particles and that nanoplates synthesized by GS2 were easier to remove compared to those synthesized by GS1, which is not well-understood. Tables S2 and S3 of Supporting Information show the $\lambda_{max}$ and extinction values of all

**TABLE 1. Data Table Showing the Percent of Nanoplates, Average Wavelength, Average Extinction, and Average Aspect Ratio of Au Nanoplates Synthesized and Purified by the Different Methods**

| | | | | | aspect ratio | |
|---|---|---|---|---|---|---|
| synthesis strategy | | % Au nanoplates | $\lambda_{max}$ (nm) | extinction at $\lambda_{max}$ | AFM only | SEM + AFM |
| growth solution 1 | as-prepared | 23 ± 7 | 549 ± 6 | 0.121 ± 0.025 | 6.1 ± 2.5 | 4.4 ± 1.9 |
| | taped | 90 ± 11 | 672 ± 15 | 0.027 ± 0.022 | 6.4 ± 2.1 | 5.3 ± 1.4 |
| | sonicated[a] | 91 ± 9 | 780 ± 47 | 0.024 ± 0.008 | 9.7 ± 2.6 | 6.5 ± 2.3 |
| growth solution 2 | as-prepared | 44 ± 8 | 627 ± 13 | 0.134 ± 0.019 | 7.1 ± 2.1 | 5.9 ± 1.7 |
| | taped | 89 ± 7 | 664 ± 23 | 0.068 ± 0.014 | 7.5 ± 2.8 | 5.6 ± 2.1 |
| | sonicated[b] | 90 ± 8 | 720 ± 12 | 0.011 ± 0.005 | 8.1 ± 2.7 | 6.9 ± 2.6 |

[a]Sonication time was 5 min. [b]Sonication time was 2−3 min. Longer times often led to more significant removal of the Au nanostructures.

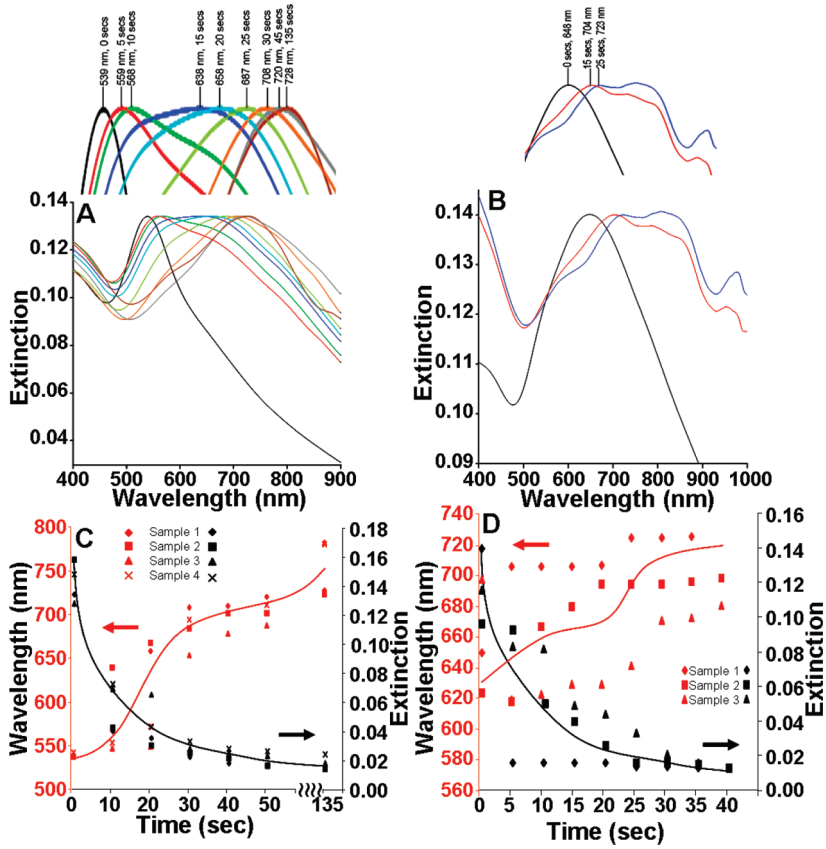


**Figure 4. Normalized LSPR spectra of Au nanostructures synthesized by (A) growth solution 1 and (B) growth solution 2 before and after sonication for the indicated times. All spectra were normalized to the absorbance of the spectrum at 0 s. The inset shows a zoom-in of the major LSPR bands with time and the $\lambda_{max}$ values. Plots of wavelength of maximum extinction ($\lambda_{max}$) on the left *y*-axis (red) and extinction at $\lambda_{max}$ on the right *y*-axis (black) as a function of sonication time for Au nanostructures synthesized by (C) growth solution 1 and (D) growth solution 2. The black and red lines were hand drawn as a guide to show the general trends.**

samples synthesized by GS1 and GS2 and purified by tape or sonication.

Table 1 also shows the average aspect ratio determined by AFM only or the combination of SEM and AFM (to measure the average width and height, respectively) of samples synthesized and purified by the different methods. The average aspect ratios of GS1 as-prepared, taped, and sonicated were 6.1 $\pm$ 2.5, 6.4 $\pm$ 2.1, and 9.7 $\pm$ 2.6 as determined by AFM and 4.4 $\pm$ 1.9, 5.3 $\pm$ 1.4, and 6.5 $\pm$ 2.3 as determined by SEM and AFM, respectively, whereas the average aspect ratio values of GS2 as-prepared, taped, and sonicated were 7.1 $\pm$ 2.1, 7.5 $\pm$ 2.8, and 8.1 $\pm$ 2.7 as determined by AFM and 5.9 $\pm$ 1.7, 5.6 $\pm$ 2.1, and 6.9 $\pm$ 2.6 as determined by SEM and AFM, respectively. In general, the average $\lambda_{max}$ values in Table 1 increase with an increase in the percent of nanoplates and increase in the average aspect ratio. For example, as-prepared nanoplate samples prepared by GS2 have a higher percent of nanoplates, higher average aspect ratio, and a larger average $\lambda_{max}$ compared to samples prepared by GS1. Taped samples have a larger percent of nanoplates, a larger or similar aspect ratio, and a larger average $\lambda_{max}$ compared to the as-prepared samples. Finally, sonicated samples have a larger average aspect ratio and larger average $\lambda_{max}$ compared to taped samples.

**Tuning the LSPR Extinction Maxima of Au Nanoplates with Sonication Time.** We obtained the LSPR spectra in Figure 3 after sonicating the samples synthesized by GS1 and GS2 for 5 and 2 min, respectively. In order to better understand the details of the removal of the spherical nanoparticles, we monitored the LSPR spectra as a function of sonication time. Figure 4A,B shows the LSPR spectra of Au nanostructures synthesized on glass using GS1 and GS2, respectively, before and after sonication for various times ranging from 0 to 135 s and 0 to 25s. The nanostructures synthesized with GS1 (Figure 4A) had an initial LSPR $\lambda_{max}$ of 539 nm at 0 s, which increased with increasing sonication time until a final value of 728 nm after 135 s. We normalized the extinction values to the initial extinction value at 0 s in Figure 4A,B in order to clearly show the shift in $\lambda_{max}$ and details of the LSPR peak with sonication time. The extinction actually decreased by a factor of 7−8 following sonication after the 135 s due to the loss of Au nanospheres and some nanoplates from the surface. Figure 4B shows the results of a similar experiment performed on Au nanostructures synthesized on glass with GS2.

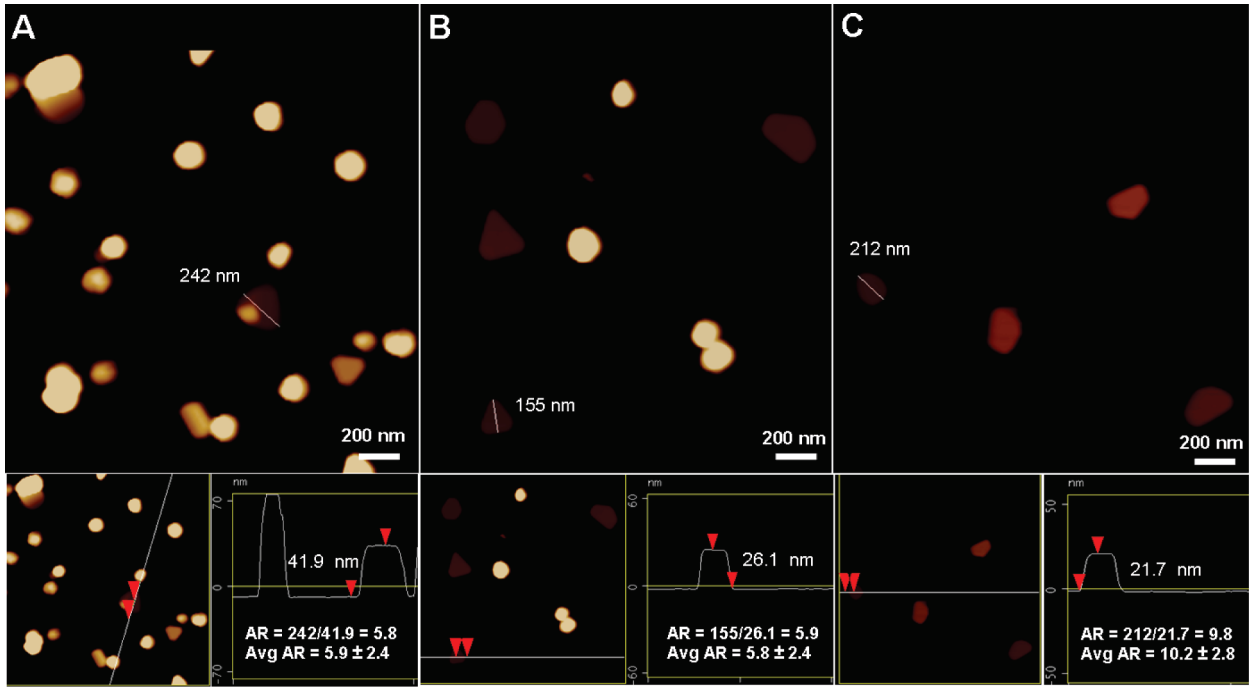


**Figure 5. AFM images of Au nanostructures synthesized by growth solution 1 before sonication (A) and after sonication for 15 s (B) and 55 s (C). The images show the width of the major axis of one nanoplate, and the inset shows the height analysis of the same nanoplate along with the calculated aspect ratio of that nanoplate. The aspect ratio of the nanoplate shown is close to the average aspect ratio of the sample based on measurements from at least 15 nanoplates as also shown in the inset. The aspect ratio is the width of the major axis divided by the nanoplate height.**

In this case, $\lambda_{max}$ was 648 nm at 0 s and gradually shifted to 704 nm after 15 s and 723 nm after 25 s of sonication. Note that while the major peak of the final spectrum was 723 nm, there was a second large peak around 780 nm and even a third peak near 900 nm. We used shorter sonication times for Au nanostructures synthesized by GS2 because, in many cases, a longer sonication time removed all of the Au from the surfaces as mentioned earlier.

Figure 4C,D shows plots of $\lambda_{max}$ (left axis) and extinction (right axis) as a function of sonication time for Au nanostructures synthesized on glass using GS1 and GS2, respectively. The general trend consistently showed an increase in $\lambda_{max}$ and decrease in extinction with increasing sonication time for both growth solutions, although the exact values with time have variability. The extinction decreased with sonication time due to the removal of spherical nanoparticles and some Au nanoplates from the surface. The increase in $\lambda_{max}$ was due to a higher population of nanoplates on the surface. Previous results showed that $\lambda_{max}$ increases for Au nanoplates as the aspect ratio increases.[32] Considering this fact, our results suggest that, with increasing sonication time, the average aspect ratio of the Au nanoplates remaining on the surface increased.

In order to determine if the average aspect ratio of the Au nanoplates increased with increasing sonication time, we obtained AFM images of the Au nanoplates at different sonication times. Figure 5 shows AFM images of Au nanostructures synthesized on a glass surface using GS1 before sonication (frame A), after sonication for 15 s (frame B), and after sonication for 55 s (frame C). As shown in Figure 1, the surface initially contained a large population of spherical nanoparticles before sonication in Figure 5A. An analysis of the aspect ratio of at least 15 different Au nanoplates showed an average of 5.9 $\pm$ 2.4. The initial $\lambda_{max}$ of this sample was 540 nm. The average aspect ratio and $\lambda_{max}$ were 5.8 $\pm$ 2.4 and 656 nm, respectively, after 15 s of sonication (frame B). Since the average aspect ratio did not change significantly, the red shift in $\lambda_{max}$ was due to the higher percentage of Au nanoplates upon removal of the spherical nanoparticles as opposed to a change in the average aspect ratio of the Au nanoplates. The average aspect ratio and $\lambda_{max}$ were 10.2 $\pm$ 2.8 and 734 nm, respectively, after 55 s of sonication (frame C). In this case, the red shift in $\lambda_{max}$ was due to further purification of the Au nanoplates and also due to the increase in the average aspect ratio of the Au nanoplates that remained on the surface.[32] The AFM determined average aspect ratio (see Table S4 in Supporting Information) and corresponding $\lambda_{max}$ are close to the calculated extinction spectra reported by Tominaga and co-workers[22] and the experimental results reported by Yun and co-workers.[32] On the basis of the AFM and LSPR data, we conclude that sonication removes spherical nanoparticles first followed by low aspect ratio nanoplates that are relatively smaller in width and larger in height. Wider and thinner plates ultimately survive the sonication and remain on the surface. These nano-

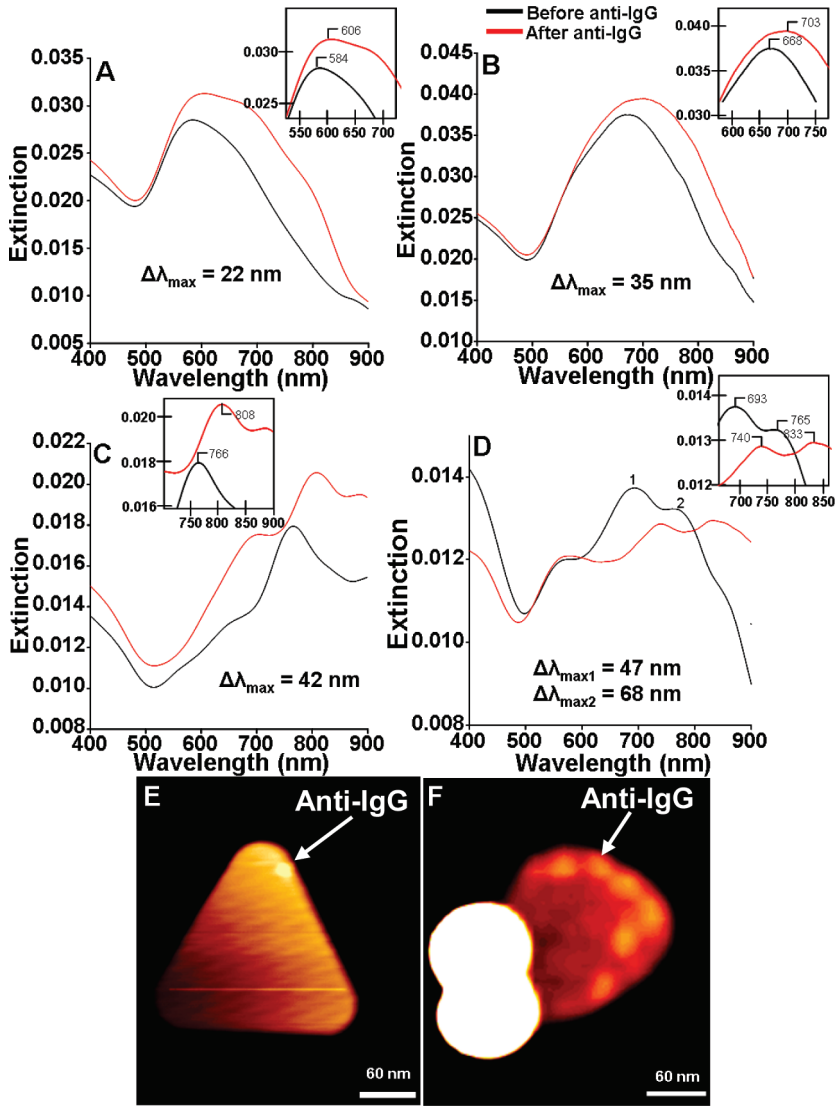


**Figure 6. LSPR spectra of Au nanoplates synthesized by growth solution 1 and purified by (A,B) taping and (C,D) sonication before (black) and after (red) functionalization with 0.26 μg/mL human anti-IgG using (A,C) 5 mM and (B,D) 6 mM place-exchanged MUA. AFM images of Au nanoplates purified by taping and functionalized with 0.26 μg/mL human anti-IgG using (E) 5 mM and (F) 6 mM place-exchanged MUA.**

plates have a larger aspect ratio with $\lambda_{max}$ values at longer wavelengths. We believe that the high aspect ratio Au nanoplates adhere best to the surface because they have a larger contact area with the surface compared to low aspect ratio nanoplates or spherical nanoparticles (aspect ratio ~1). At this point, we do not have any evidence that the sonication procedure directly alters the size and shape of the nanoplates, although this is a possibility due to the heat generated.[50]

**LSPR Response of Au Nanoplates to Anti-IgG Binding.** We used our previously published method to attach anti-IgG selectively to the edge sites of the Au nanoplates synthesized using GS1 and GS2 and purified by taping and sonication.[18] With this procedure, we attached human anti-IgG from a 0.26 μg/mL solution onto the Au nanoplates by an amide coupling reaction to the carboxylic acid groups of mercaptoundecanoic acid (MUA), which was place-exchanged from a 5 or 6 mM solution onto Au nanoplates functionalized first with mercaptoethanol (ME) (see Methods for full details).[18] We measured the collective LSPR spectrum of the Au nanoplates from the same exact location on carefully marked glass substrates before and after attachment of anti-IgG. Figure 6 shows the LSPR spectra of glass samples containing Au nanoplates synthesized by GS1 and purified by the tape procedure (frame A and frame B) or by sonication (frame C and frame D) before and after anti-IgG functionalization using a 5 mM (frame A and frame C) and 6 mM (frame B and frame D) place-exchanged MUA linker. We previously showed that attachment of anti-IgG to MUA that was place-exchanged from a 5 and 6 mM solution led to a greater amount of anti-IgG on the edge sites for the latter.[18] The LSPR spectra of nanoplates purified by taping in Figure 6A,B show a shift in $\lambda_{max}$ of 22 and 35 nm for attachment of anti-IgG to 5 and 6 mM exchanged MUA, respectively,

**TABLE 2. Initial $\lambda_{max}$ ($\lambda_{max,init}$) and Response to Human Anti-IgG Binding of the Au Nanoplate Samples Synthesized, Purified, and Functionalized by Different Methods**

| | | 5 mM MUA | | 6 mM MUA | |
|---|---|---|---|---|---|
| synthesis strategy | | $\lambda_{max,init}$ (nm) | $\Delta\lambda_{max}$ (nm) | $\lambda_{max,init}$ (nm) | $\Delta\lambda_{max}$ (nm) |
| growth solution 1 | as-prepared | 547 ± 12 | 6 ± 3 | 545 ± 4 | 9 ± 1 |
| | taped | 644 ± 52 | 23 ± 1 | 675 ± 54 | 32 ± 3 |
| | sonicated | 766 ± 70 | 49 ± 13 | 704 ± 8 | 53 ± 4 |
| growth solution 2 | as-prepared | 624 ± 9 | 16 ± 2 | 642 ± 36 | 22 ± 3 |

while those of nanoplates purified by sonication in Figure 6C,D show a shift in $\lambda_{max}$ of 42 and 47−68 nm for attachment of anti-IgG to 5 and 6 mM exchanged MUA, respectively. In three of the four cases, the extinction also increased, but we showed previously that this is less reproducible than the shift in $\lambda_{max}$.[18] In both cases, the larger shift for the 6 mM MUA samples shows that more anti-IgG attached to the edges of the nanoplates compared to the 5 mM samples. The sonicated samples showed a larger shift in $\lambda_{max}$ upon anti-IgG binding compared to taped samples due to the larger initial $\lambda_{max}$ value for these nanostructures, as it has been shown that the sensitivity to a refractive index change in the environment increases with increasing initial $\lambda_{max}$.[81,83−85] This is also evident from the fact that peak 2 in Figure 6D was more sensitive to anti-IgG binding compared to peak 1 in the same spectrum. Control experiments with pure ME treated samples showed $\Delta\lambda_{max}$ of only 1 nm (Figure S2 of Supporting Information) when treated with anti-IgG. We repeated this important control experiment several times with similar results, which confirms that (1) human anti-IgG covalently binds to the MUA linker and (2) we were successful at monitoring the same location of the sample before and after functionalization.

Figure 6E,F shows AFM images of two Au nanoplates synthesized on Si/$SiO_x$ using GS1, purified by taping, and then functionalized with anti-IgG by coupling to 5 and 6 mM place-exchanged MUA, respectively. The darkest regions correspond to the underlying Si/$SiO_x$ substrate, the intermediate shade corresponds to the triangular or circular Au nanoplates, and the bright regions on top of the nanoplates correspond to the anti-IgG. The very big bright spot in Figure 6F is a large spherical nanoparticle that was not removed during taping. The AFM images confirm that anti-IgG attached preferentially to the edges of the Au nanoplates and that the coverage increased with increasing MUA concentration, as shown previously for nonpurified nanoplate samples.[18] The AFM is consistent with the fact that the $\lambda_{max}$ shift was largest for the anti-IgG attached to 6 mM place-exchanged MUA.

Table 2 shows the average initial $\lambda_{max}$ ($\lambda_{max,init}$) and shift in $\lambda_{max}$ ($\Delta\lambda_{max}$) of the Au nanostructures synthesized by GS1 and GS2 before (as-prepared) and after purification by tape and sonication for the nanostructures synthesized by GS1. For nanostructures synthesized by GS1 and functionalized with human anti-IgG through 5 mM place-exchanged MUA, the $\Delta\lambda_{max}$ increased in the order of as-prepared (6 ± 3 nm) < taped (23 ± 1 nm) < sonicated (49 ± 13 nm). On the basis of the data in Tables 1 and 2, the $\Delta\lambda_{max}$ increases with increasing percentage of Au nanoplates and increasing initial $\lambda_{max,init}$ of the nanoplates. The as-prepared sample had 26% Au nanoplates on the sample and the lowest $\lambda_{max,init}$ (547 nm), while the sonicated sample had ~90% Au nanoplates and largest $\lambda_{max,init}$ of 766 nm. The $\Delta\lambda_{max}$ also increased with increasing percentage of Au nanoplates and $\lambda_{max,init}$ for samples functionalized by human anti-IgG through 6 mM place-exchanged MUA. The $\Delta\lambda_{max}$ was about 50% larger when compared to the 5 mM place-exchanged samples in all cases except for those synthesized by GS1 and sonicated. The general increase in $\Delta\lambda_{max}$ for the 6 mM samples occurred because of the larger number of anti-IgG on the nanoplate surface as determined by AFM. The smaller difference between 6 and 5 mM in the case of the sonicated samples synthesized by GS1 could be due to the larger $\lambda_{max,init}$ for the 5 mM samples (by 62 nm), which makes those nanoplates more sensitive to refractive index changes. The magnitude of $\Delta\lambda_{max}$ for the as-prepared GS2 samples lies between the as-prepared GS1 samples and taped GS1 samples, consistent with the percentage of Au nanoplates and $\lambda_{max,init}$ for this sample shown in Tables 1 and 2. Importantly, our results show that samples of purified nanoplates, by sonication or taping, exhibit a significantly larger LSPR response to protein binding compared to the as-prepared samples containing mostly spherical nanoparticles.

**Sensing IgG.** We performed a preliminary test on the use of surface-attached Au nanoplates synthesized by GS1, purifed by taping, and functionalized with human anti-IgG for the detection of human IgG. Figure 7 shows the LSPR spectra of the Au nanoplates before (black spectrum) and after (red spectrum) edge functionalization with human anti-IgG using 6 mM place-exchanged MUA as the linker. Attachment of anti-IgG led to a shift from 624 to 657 nm ($\Delta\lambda_{max}$ = 33 nm) and 763 to 800 nm ($\Delta\lambda_{max}$ = 37 nm) for the first and second LSPR peaks, respectively. These shifts are consistent with those observed for other taped samples synthesized by GS1, as shown in Figure 6 and Table 2. Subsequent exposure to a 10 pg/mL solution of IgG led to a further shift from

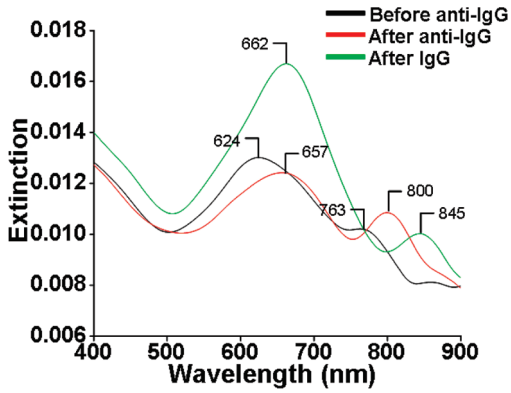


**Figure 7. LSPR spectra showing a glass sample coated with tape purified Au nanostructures synthesized by growth solution 1 before functionalization with human anti-IgG (black), after functionalization with human anti-IgG using 6 mM place-exchanged MUA (red), and after exposure to 10 pg/mL human IgG (green).**

657 to 662 nm ($\Delta\lambda_{max} = 7$ nm) and 800 to 845 nm ($\Delta\lambda_{max} = 45$ nm) for the first and second LSPR peaks (green spectrum), respectively. Interestingly, the extinction value increased dramatically for the first peak and slightly decreased for the second peak, while the second peak exhibited a much larger shift in $\lambda_{max}$. These two different populations of Au nanoplates on the same sample (peaks 1 and 2) showed similar results upon anti-IgG binding but drastically different responses to IgG. The reason is not clear at this time. This interesting phenomenon can only be elucidated by correlating LSPR spectroscopy data with AFM imaging of the protein binding location at the single nanoplate level. This is an exciting topic that we will explore in the future. Importantly, this sample exhibited a much larger $\Delta\lambda_{max}$ in response to a 10 times lower IgG concentration (10 pg/mL or $<$1 pM) compared to our previous work on samples containing a majority of Au nanospheres.[18] This is among the lowest concentration detected by LSPR for proteins to date.[86] The detailed aspects of human IgG sensing with purified Au nanoplates, including kinetics, sensitivity, and limit of detection, will be described separately.

**Refractive Index Sensitivity.** We performed refractive index sensitivity studies on a nonpurified sample synthesized by GS1 (containing mostly spherical nanoparticles) and on three sample synthesized by GS1 and purified by sonication. Figure S3 of Supporting Information shows the LSPR spectra obtained in air, toluene, 2-propanol, water, and then back in air. The $\lambda_{max}$ of the LSPR band increased with increasing refractive index (RI) of the solvent as expected. Also, the spectrum in air before exposure to the solvents matches the spectrum after exposure to the different solvents, indicating that the nanoplate samples were stable and the spectra were from the same region of the glass sample. Importantly, we found that the extinction intensity increased in some cases, as we also observed for anti-IgG or IgG binding to the Au nanoplates. Figure S4 (Supporting Information) shows plots of the change in $\lambda_{max}$ as a function of the RI of the solvent. From the slope, the RI sensitivity was 89 nm/RIU for the nonpurified sample with a $\lambda_{max}$ of 539 nm and 195 and 302 nm/RIU for the purified nanoplate samples with a $\lambda_{max}$ of 677 and 828 nm, respectively. As expected, the RI sensitivity increased as the initial $\lambda_{max}$ of the LSPR band increased. In addition, toluene has a RI closest to that expected for proteins such as anti-IgG; therefore, the 90−150 nm shift, depending on the $\lambda_{max}$, represents the upper limit of the $\lambda_{max}$ shift for a full coverage of anti-IgG on the nanoplate surface. The fact that we observe shifts of 50 nm in some cases for anti-IgG bound to nanoplate edge sites, which is one-third to one-half of the maximum signal, shows that the edge sites are highly sensitive since the nanoplate surface is not nearly one-third or one-half covered by the anti-IgG based on the AFM images.

## CONCLUSIONS

We demonstrated the seed-mediated synthesis of Au nanoplates directly on surfaces using two different growth solutions and selectively removed Au nanospheres by tape or sonication to form samples with ~90% Au nanoplates. We believe that the smooth, flat morphology of the Au nanoplates provides a larger contact area with the surface that allows them to adhere more strongly compared to Au spheres. The different synthesis and purification strategies led to different $\lambda_{max}$ values for the Au nanoplate samples, ranging from 549 up to 780 nm, and the LSPR $\lambda_{max}$ could be tuned by altering the sonication time. The $\lambda_{max}$ value increases with increasing purity of the nanoplates and increasing aspect ratio of the plates that remain on the surface. The $\lambda_{max}$ of purified nanoplates from the LSPR spectrum after edge functionalization with human anti-IgG shifted by 22 up to 68 nm, which is 4−8 times larger compared to samples dominated by Au nanospheres, depending on the amount of anti-IgG attached and the purification strategy. Au nanoplates synthesized by GS1 and sonicated for 5 min had the largest initial $\lambda_{max}$ and largest shift upon anti-IgG binding. In addition, a tape purified Au nanoplate sample edge-functionalized with anti-IgG detected 10 pg/mL of IgG with a large 45 nm shift for the largest $\lambda_{max}$ LSPR band. This shows that these purified Au nanoplates have great promise for use in highly sensitive protein detection. This work is important because our synthesis and purification strategy involves simple benchtop procedures that do not require high vacuum evaporation or sputtering, lithography, or other complex or expensive methods. Because the growth is directly on surfaces, we eliminate the need for assembling Au nanoplates onto a surface from solution. The protein functionalization strategy importantly shows that the LSPR spectrum of Au nanoplates is highly sensitive to the bind-

ing of just a few protein molecules on the edge, which may also be useful for monitoring molecular binding to metal nanostructure edge sites by surface-enhanced Raman spectroscopy (SERS).

## METHODS

**Chemicals.** Citric acid trisodium salt was purchased from Bio-rad Laboratories. L-Ascorbic acid (99%), sodium borohydride (98.5%), cetyltrimethylammonium bromide (CTAB), 11-mercaptoundecanoic acid (MUA), 2-mercaptoethanol (ME), and *N*-hydroxysuccinimide (NHS) were purchased from Sigma-Aldrich. 1-Ethyl-3-(3-dimethylaminopropyl)carbodiimide (EDC) was purchased from Pierce, and 95% mercaptopropyltrimethoxysilane (MPTMS) was purchased from Alfa Aesar. Antibody anti-human-IgG and human IgG were purchased from Sigma-Aldrich.

**Synthesis of Au Nanostructures Directly on Surfaces.** Au nanostructures were synthesized directly on glass microscope slides and $Si/SiO_x$ surfaces by a seed-mediated growth procedure as described previously.[18] Glass and silicon slides were first cut and cleaned in piranha solution (1:3 $H_2O_2/H_2SO_4$) for 10−15 min. **(Caution: this solution, piranha, is a strong oxidizing agent that reacts violently with organics.)** After being rinsed with water and dried under a stream of $N_2$, the substrates were functionalized with MPTMS by heating them just below boiling in a solution containing 10 mL of 2-propanol, 100 μL of MPTMS, and a few drops of water for about 30 min. After being rinsed with 2-propanol and dried under $N_2$, the MPTMS-functionalized silicon and glass slides were placed in an aqueous solution of 3−5 nm diameter citrate-stabilized Au nanoparticles ("seeds") for 15 min, which leads to their attachment to the thiol functionality of MPTMS through a strong Au−thiolate interaction. (The gold seed solution was prepared by adding 0.5 mL of 0.01 M sodium citrate trisodium salt and 0.05 mL of 0.01 M $HAuCl_4$ to 19 mL of water while stirring and then adding 0.6 mL of ice cold 0.1 M sodium borohydride while stirring. The seed solution was allowed to stir for at least 2 h prior to use.) After rinsing with water, the substrates containing immobilized Au seed nanoparticles were then placed in a freshly prepared solution termed growth solution 1 (GS1), which contained 9 mL of 0.1 M cetyltrimethylammonium bromide (CTAB), 450 μL of 0.01 M $HAuCl_4$, and 50 μL of 0.1 M ascorbic acid for 1 h. Alternatively, the Au-seeded substrates were placed in growth solution 2 (GS2), which contained 9 mL of 0.016 M CTAB, 450 μL of 0.01 M $HAuCl_4$, and 150 μL of 0.2 M ascorbic acid. In both cases, this leads to the preferential reduction of Au from solution onto the surface-attached Au nanoparticle seeds *via* ascorbic acid, leading to the growth of the 3−5 nm diameter Au nanoparticles into larger Au nanostructures directly on the surface. The samples were rinsed with water and dried under nitrogen before further use. The source of the CTAB was Aldrich (95%) in both growth solutions, which was critical for synthesizing samples with a large population of nanoplates as described previously.[79]

**Nanoplate Purification.** ***Purification by Tape:*** We used Scotch brand magic adhesive tape to preferentially remove the spherical nanoparticles from the glass or $Si/SiO_x$ surface. The tape was placed on the substrate, pressed gently with one finger, and then slowly peeled back at an approximately 90° angle. In the case of glass, the procedure was performed on both sides.

***Purification by Sonication:*** We used a Bransonic ultrasonic cleaner with a 935 W input and 250 W output puissance HF to remove the spherical nanoparticles from substrates containing Au nanostructures. The substrate was placed in a glass vial containing 10 mL of nanopure water and then placed in the ultrasonicator for 2−5 min as indicated. The substrate was removed from the vial, washed thoroughly with nanopure water, and dried under nitrogen.

**Functionalizing the Au Nanoplates with Anti-IgG.** We controllably attached anti-IgG to the edges of Au nanoplates using our procedure described previously.[18] The samples purified by tape were placed in a solution of dichloromethane for 6−7 h to remove any tape residue from the surface. We then placed the sample in a 1 mM ethanol solution of mercaptoethanol (ME) overnight, rinsed thoroughly with ethanol, dried under $N_2$, and then exchanged the ME monolayer with MUA by placing the sample into a 5 or 6 mM ethanol solution of MUA for 4 h. We again rinsed thoroughly with ethanol, dried under $N_2$, and then placed the sample in an aqueous solution of 2 mM 1-ethyl-3-(3-dimethylaminopropyl)carbodiimide (EDC) and 5 mM *N*-hydroxysuccinimide (NHS) for 1 h. After being rinsed with water and dried under $N_2$, the sample was placed into a 0.26 μg/mL aqueous pH 7.4 phosphate buffered solution of human anti-IgG for 12−15 h in the refrigerator, rinsed with phosphate buffered saline and water, and dried under $N_2$.

**IgG Sensing.** Human IgG sensing was performed by placing the sample of human anti-IgG-functionalized Au nanoplates in a pH 7.4 phosphate buffered aqueous saline solution containing 0.01 ng/mL of human IgG overnight in the refrigerator before rinsing with pH 7.4 phosphate buffered saline and water and drying under $N_2$.

**Instrumentation.** UV−vis spectra were obtained with a Varian Cary 50 BIO UV−vis spectrophotometer. We reduced the noise in all of the extinction spectra by using the smooth operation in the Varian software with a filter size of 101. The changes in wavelength of maximum extinction ($\lambda_{max}$) were calculated by allowing the software to chose the $\lambda_{max}$ of the smoothed spectra. Atomic force microscopy (AFM) images were obtained with a Veeco Digital Instruments Nanoscope IIIa Multimode scanning probe microscope (Santa Barbara, CA) using a Si tip in tapping mode. Scanning electron microscopy (SEM) images were obtained with a FEI-NOVA-600 NANO SEM.

*Acknowledgment.* We gratefully acknowledge the National Science Foundation (CHE-0848883) for full financial support of this research.

*Supporting Information Available:* Data tables showing the average width, height, aspect ratio, wavelength, and extinction with standard deviations for samples synthesized by GS1 and GS2 before and after purification by tape and sonication, UV−vis spectra of several samples synthesized by GS1 and purified by sonication, AFM analysis of Au nanoplates at different stages of sonication on all samples, control LSPR spectra of a pure ME sample, and RI sensitivity of samples synthesized by GS1 and purified by sonication. This material is available free of charge *via* the Internet at http://pubs.acs.org.

## REFERENCES AND NOTES

1. Jain, P. K.; Huang, X.; El-Sayed, I. H.; El-Sayed, M. A. Noble Metals on the Nanoscale: Optical and Photothermal Properties and Some Applications in Imaging, Sensing, Biology, and Medicine. *Acc. Chem. Res.* **2008**, *41*, 1578–1586.
2. Stewart, M. E.; Anderton, C. R.; Thompson, L. B.; Maria, J.; Gray, S. K.; Rogers, J. A.; Nuzzo, R. G. Nanostructured Plasmonic Sensors. *Chem. Rev.* **2008**, *108*, 494–521.
3. Haes, A. J.; Hall, W. P.; Chang, L.; Klein, W. L.; Van Duyne, R. P. A Localized Surface Plasmon Resonance Biosensor: First Steps toward an Assay for Alzheimer's Disease. *Nano Lett.* **2004**, *4*, 1029–1034.
4. Marinakos, S. M.; Chen, S.; Chilkoti, A. Plasmonic Detection of a Model Analyte in Serum by a Gold Nanorod Sensor. *Anal. Chem.* **2007**, *79*, 5278–5283.
5. Mayer, K. M.; Lee, S.; Liao, H.; Rostro, B. C.; Fuentes, A.; Scully, P. T.; Nehl, C. L.; Hafner, J. H. A Label-Free Immunoassay Based upon Localized Surface Plasmon Resonance of Gold Nanorods. *ACS Nano* **2008**, *2*, 687–692.
6. Bendikov, T. A.; Rabinkov, A.; Karakouz, T.; Vaskevich, A.; Rubinstein, I. Biological Sensing and Interface Design in Gold Island Film Based Localized Plasmon Transducers. *Anal. Chem.* **2008**, *80*, 7487–7498.

7. Nath, N.; Chilkoti, A. A Colorimetric Gold Nanoparticle Sensor To Interrogate Biomolecular Interactions in Real Time on a Surface. *Anal. Chem.* **2002**, *74*, 504–509.
8. Nath, N.; Chilkoti, A. Label-Free Biosensing by Surface Plasmon Resonance of Nanoparticles on Glass: Optimization of Nanoparticle Size. *Anal. Chem.* **2004**, *76*, 5370–5378.
9. Gish, D. A.; Nsiah, F.; McDermott, M. T.; Brett, M. J. Localized Surface Plasmon Resonance Biosensor Using Silver Nanostructures Fabricated by Glancing Angle Deposition. *Anal. Chem.* **2007**, *79*, 4228–4232.
10. Sannomiya, T.; Hafner, C.; Voros, J. *In Situ* Sensing of Single Binding Events by Localized Surface Plasmon Resonance. *Nano Lett.* **2008**, *8*, 3450–3455.
11. Schultz, S.; Smith, D. R.; Mock, J. J.; Schultz, D. A. Single-Target Molecule Detection with Nonbleaching Multicolor Optical Immunolabels. *Proc. Natl. Acad. Sci. U.S.A.* **2000**, *97*, 996–1001.
12. Sönnichsen, C.; Reinhard, B. M.; Liphardt, J.; Alivisatos, A. P. A Molecular Ruler Based on Plasmon Coupling of Single Gold and Silver Nanoparticles. *Nat. Biotechnol.* **2005**, *23*, 741–745.
13. Karakouz, T.; Vaskevich, A.; Rubinstein, I. Polymer-Coated Gold Island Films as Localized Plasmon Transducers for Gas Sensing. *J. Phys. Chem. B* **2008**, *112*, 14530–14538.
14. Kim, S.; Cheng, N.; Jeong, J.-R.; Jang, S.-G.; Yang, S.-M.; Huck, W. T. S. Localized Surface Plasmon Resonance (LSPR) Sensitivity of Au Nanodot Patterns To Probe Solvation Effects in Polyelectrolyte Brushes. *Chem. Commun.* **2008**, 3666–3668.
15. Kim, Y.; Johnson, R. C.; Hupp, J. T. Gold Nanoparticle-Based Sensing of "Spectroscopically Silent" Heavy Metal Ions. *Nano Lett.* **2001**, *1*, 165–167.
16. Russell, L. E.; Pompano, R. R.; Kittredge, K. W.; Leopold, M. C. Assembled Nanoparticle Films with Crown Ether−Metal Ion Sandwiches as Sensing Mechanisms for Metal Ions. *J. Mater. Sci.* **2007**, *42*, 7100–7108.
17. Nusz, G. J.; Curry, A. C.; Marinakos, S. M.; Wax, A.; Chilkoti, A. Rational Selection of Gold Nanorod Geometry for Label-Free Plasmonic Biosensors. *ACS Nano* **2009**, *3*, 795–806.
18. Beeram, S. R.; Zamborini, F. P. Selective Attachment of Antibodies to the Edge Sites of Gold Nanostructures for Enhanced Localized Surface Plasmon Resonance Biosensing. *J. Am. Chem. Soc.* **2009**, *131*, 11689–11691.
19. Haes, A. J.; Zou, S.; Schatz, G. C.; Van Duyne, R. P. Nanoscale Optical Biosensor: Short Range Distance Dependence of the Localized Surface Plasmon Resonance of Noble Metal Nanoparticles. *J. Phys. Chem. B* **2004**, *108*, 6961–6968.
20. Nelayah, J.; Kociak, M.; Stephan, O.; Abajo, F. J. G. D.; Tence, M.; Henrard, L.; Taverna, D.; Pastoriza-Santos, I.; Liz-Marzan, L. M.; Colliex, C. Mapping Surface Plasmons on a Single Metallic Nanoparticle. *Nat. Phys.* **2007**, *3*, 348–353.
21. Zhou, M.; Chen, S.; Zhao, S.; Ma, H. Preparation of Gold Nanoplates by an Electrochemical Method. *Chem. Lett.* **2005**, *34*, 1670–1671.
22. Takezaki, M.; Kida, R.; Kato, Y.; Tominaga, T. Preparations of Triangular Gold Nanoplates by Chemical and Photoreduction Methods. *Chem. Lett.* **2009**, *38*, 1022–1023.
23. Zhou, Y.; Wang, C. Y.; Zhu, Y. R.; Chen, Z. Y. A Novel Ultraviolet Irradiation Technique for Shape-Controlled Synthesis of Gold Nanoparticles at Room Temperature. *Chem. Mater.* **1999**, *11*, 2310–2312.
24. Kan, C.; Wang, G.; Zhu, X.; Li, C.; Cao, B. Structure and Thermal Stability of Gold Nanoplates. *Appl. Phys. Lett.* **2006**, *88*, 719041–719043.
25. Kim, F.; Connor, S.; Song, H.; Kuykendall, T.; Yang, P. Platonic Gold Nanocrystals. *Angew. Chem., Int. Ed.* **2004**, *43*, 3673–3677.
26. Lee, J.-H.; Kamada, K.; Enomoto, N.; Hojo, J. Polyhedral Gold Nanoplate: High Fraction Synthesis of Two-Dimensional Nanoparticles through Rapid Heating Process. *Cryst. Growth Des.* **2008**, *8*, 2638–2645.
27. Sun, X.; Dong, S.; Wang, E. Large-Scale Synthesis of Micrometer-Scale Single-Crystalline Au Plates of Nanometer Thickness by a Wet-Chemical Route. *Angew. Chem., Int. Ed.* **2004**, *43*, 6360–6363.
28. Sun, X.; Dong, S.; Wang, E. High-Yield Synthesis of Large Single-Crystalline Gold Nanoplates through a Polyamine Process. *Langmuir* **2005**, *21*, 4710–4712.
29. Shankar, S. S.; Rai, A.; Ankamwar, B.; Singh, A.; Ahmad, A.; Sastry, M. Biological Synthesis of Triangular Gold Nanoprisms. *Nat. Mater.* **2004**, *3*, 482–488.
30. Xiong, Y.; Washio, I.; Chen, J.; Cai, H.; Li, Z.-Y.; Xia, Y. Poly(vinyl pyrrolidone): A Dual Functional Reductant and Stabilizer for the Facile Synthesis of Noble Metal Nanoplates in Aqueous Solutions. *Langmuir* **2006**, *22*, 8563–8570.
31. Yamamoto, M.; Kashiwagi, Y.; Sakata, T.; Mori, H.; Nakamoto, M. Synthesis and Morphology of Star-Shaped Gold Nanoplates Protected by Poly(*N*-vinyl-2-pyrrolidone). *Chem. Mater.* **2005**, *17*, 5391–5393.
32. Ah, C. S.; Yun, Y. J.; Park, H. J.; Kim, W.-J.; Ha, D. H.; Yun, W. S. Size-Controlled Synthesis of Machinable Single Crystalline Gold Nanoplates. *Chem. Mater.* **2005**, *17*, 5558–5561.
33. Huang, W.-L.; Chen, C.-H.; Huang, M. H. Investigation of the Growth Process of Gold Nanoplates Formed by Thermal Aqueous Solution Approach and the Synthesis of Ultra-Small Gold Nanoplates. *J. Phys. Chem. C* **2007**, *111*, 2533–2538.
34. Wang, J.; Wang, Z. Rapid Synthesis of Hexagon-Shaped Gold Nanoplates by Microwave Assistant Method. *Mater. Lett.* **2007**, *61*, 4149–4151.
35. Luo, Y. Large-Scale Preparation of Single Crystalline Gold Nanoplates. *Mater. Lett.* **2007**, *61*, 1346–1349.
36. Baigorri, R.; Garcia-Mina, J. M.; Aroca, R. F.; Alvarez-Puebla, R. A. Optical Enhancing Properties of Anisotropic Gold Nanoplates Prepared with Different Fractions of a Natural Humic Substance. *Chem. Mater.* **2008**, *20*, 1516–1521.
37. Bai, X.; Zheng, L.; Li, N.; Dong, B.; Liu, H. Synthesis and Characterization of Microscale Gold Nanoplates Using Langmuir Monolayers of Long-Chain Ionic Liquid. *Cryst. Growth Des.* **2008**, *8*, 3840–3846.
38. Porel, S.; Singh, S.; Radhakrishnan, T. P. Polygonal Gold Nanoplates in a Polymer Matrix. *Chem. Commun.* **2005**, 2387–2389.
39. Li, Z.; Liu, Z.; Zhang, J.; Han, B.; Du, J.; Gao, Y.; Jiang, T. Synthesis of Single-Crystal Gold Nanosheets of Large Size in Ionic Liquids. *J. Phys. Chem. B* **2005**, *109*, 14445–14448.
40. Wang, L.; Chen, X.; Zhan, J.; Chai, Y.; Yang, C.; Xu, L.; Zhuang, W.; Jing, B. Synthesis of Gold Nano- and Microplates in Hexagonal Liquid Crystals. *J. Phys. Chem. B* **2005**, *109*, 3189–3194.
41. Simakin, A. V.; Voronov, V. V.; Shafeev, G. A.; Brayner, R.; Bonzon-Verduraz, F. Nanodisks of Au and Ag Produced by Laser Ablation in Liquid Environment. *Chem. Phys. Lett.* **2001**, *348*, 182–186.
42. Zhang, J.; Liu, H.; Zhan, P.; Wang, Z.; Ming, N. Controlling the Growth and Assembly of Silver Nanoprisms. *Adv. Funct. Mater.* **2007**, 1558–1566.
43. Pastoriza-Santos, I.; Liz-Marzan, L. M. Synthesis of Silver Nanoprisms in DMF. *Nano Lett.* **2002**, *2*, 903–905.
44. Bastys, V.; Pastoriza-Santos, I.; Rodriguez-Gonzalez, B.; Vaisnoras, R.; Liz-Marzan, L. M. Formation of Silver Nanoprisms with Surface Plasmons at Communication Wavelengths. *Adv. Funct. Mater.* **2006**, *16*, 766–773.
45. Jin, R.; Cao, Y.; Kelly, K. L.; Zheng, J. G.; Schatz, G. C.; Mirkin, C. A. Photoinduced Conversion of Silver Nanospheres to Nanoprisms. *Science* **2001**, *294*, 1901–1903.
46. Jin, R.; Cao, Y. C.; Hao, E.; Metraux, G. S.; Schatz, G. C.; Mirkin, C. A. Controlling Anisotropic Nanoparticle Growth through Plasmon Excitation. *Nature* **2003**, *425*, 487–490.
47. Xue, C.; Metraux, G. S.; Millstone, J. E.; Mirkin, C. A. Mechanistic Study of Photomediated Triangular Silver Nanoprism Growth. *J. Am. Chem. Soc.* **2008**, *130*, 8337–8344.

48. Xue, C.; Mirkin, C. A. pH-Switchable Silver Nanoprism Growth Pathways. *Angew. Chem., Int. Ed.* **2007**, *46*, 2036–2038.
49. Metraux, G. S.; Mirkin, C. A. Rapid Thermal Synthesis of Silver Nanoprisms with Chemically Tailorable Thickness. *Adv. Mater.* **2005**, *17*, 412–415.
50. Tang, B.; An, J.; Zheng, X.; Xu, S.; Li, D.; Zhou, J.; Zhao, B.; Xu, W. Silver Nanodisks with Tunable Size by Heat Aging. *J. Phys. Chem. C* **2008**, *112*, 18361–18367.
51. An, J.; Tang, B.; Ning, X.; Zhou, J.; Xu, S.; Zhao, B.; Xu, W.; Corredor, C.; Lombardi, J. R. Photoinduced Shape Evolution: From Triangular to Hexagonal Silver Nanoplates. *J. Phys. Chem. C* **2007**, *111*, 18055–18059.
52. Tang, B.; Xu, S.; An, J.; Zhao, B.; Xu, W. Photoinduced Shape Conversion and Reconstruction of Silver Nanoprisms. *J. Phys. Chem. C* **2009**, *113*, 7025–7030.
53. Zhang, Q.; Ge, J.; Pham, T.; Goebl, J.; Hu, Y.; Lu, Z.; Yin, Y. Reconstruction of Silver Nanoplates by UV Irradiation: Tailored Optical Properties and Enhanced Stability. *Angew. Chem., Int. Ed.* **2009**, *48*, 3516–3519.
54. Aherne, D.; Ledwith, D. M.; Gara, M.; Kelly, J. M. Optical Properties and Growth Aspects of Silver Nanoprisms Produced by a Highly Reproducible and Rapid Synthesis at Room Temperature. *Adv. Funct. Mater.* **2008**, *18*, 2005–2016.
55. Chen, S.; Carroll, D. L. Synthesis and Characterization of Truncated Triangular Silver Nanoplates. *Nano Lett.* **2002**, *2*, 1003–1007.
56. Guo, Z.; Zhang, Y.; Mao, Y.; Huang, L.; Gu, N. Synthesis of Microsized Gold Nanoplates by a Self-Seeding Method in Ethanol Solution. *Mater. Lett.* **2006**, *60*, 3522–3525.
57. Ha, T. H.; Koo, H.-J.; Chung, B. H. Shape-Controlled Synthesis of Gold Nanoprisms and Nanorods Influenced by Specific Adsorption of Halide Ions. *J. Phys. Chem. C* **2007**, *111*, 1123–1130.
58. Jiang, X.; Zeng, Q.; Yu, A. A Self-Seeding Coreduction Method for Shape Control of Silver Nanoplates. *Nanotechnology* **2006**, *17*, 4929–4935.
59. Millstone, J. E.; Metraux, G. S.; Mirkin, C. A. Controlling the Edge Length of Gold Nanoprisms *via* a Seed-Mediated Approach. *Adv. Funct. Mater.* **2006**, *16*, 1209–1214.
60. Millstone, J. E.; Park, S.; Shuford, K. L.; Qin, L.; Schatz, G. C.; Mirkin, C. A. Observation of a Quadrupole Plasmon Mode for a Colloidal Solution of Gold Nanoprisms. *J. Am. Chem. Soc.* **2005**, *127*, 5312–5313.
61. Bae, Y.; Kim, N. H.; Kim, M.; Lee, K. Y.; Han, S. W. Anisotropic Assembly of Ag Nanoprisms. *J. Am. Chem. Soc.* **2008**, *130*, 5432–5433.
62. Aslan, K.; Lakowicz, J. R.; Geddes, C. D. Rapid Deposition of Triangular Nanoplates on Planar Surfaces: Application to Metal-Enhanced Fluorescence. *J. Phys. Chem. B* **2005**, *109*, 6247–6251.
63. Sajanlal, P. R.; Pradeep, T. Electric-Field Assisted Growth of Highly Uniform and Oriented Gold Nanotriangles on Conducting Glass Substrates. *Adv. Mater.* **2008**, *20*, 980–983.
64. Sun, Y. Direct Growth of Dense, Pristine Metal Nanolates with Well-Controlled Dimensions on Semiconductor Substrates. *Chem. Mater.* **2007**, *19*, 5845–5847.
65. Umar, A. A.; Oyama, M. Formation of Gold Nanoplates on Indium Tin Oxide Surface: Two-Dimensional Crystal Growth from Gold Nanoseed Particles in the Presence of Poly(vinylpyrrolidone). *Cryst. Growth Des.* **2006**, *6*, 818–821.
66. Umar, A. A.; Oyama, M.; Salleh, M. M.; Majlis, B. Y. Formation of High-Yield Gold Nanoplates on the Surface: Effective Two-Dimensional Crystal Growth of Nanoseed in the Presence of Poly(vinylpyrrolidone) and Cetyltrimethylammonium Bromide. *Cryst. Growth Des.* **2009**, *9*, 2835–2840.
67. Haynes, C. L.; Van Duyne, R. P. Nanosphere Lithography: A Versatile Nanofabrication Tool for Studies of Size-Dependent Nanoparticle Optics. *J. Phys. Chem. B* **2001**, *105*, 5599–5611.
68. Chan, G. H.; Zhao, J.; Hicks, E. M.; Schatz, G. C.; Van Duyne, R. P. Plasmonic Properties of Copper Nanoparticles Fabricated by Nanosphere Lithography. *Nano Lett.* **2007**, *7*, 1947–1952.
69. Chan, G. H.; Zhao, J.; Schatz, G. C.; Van Duyne, R. P. Localized Surface Plasmon Resonance Spectroscopy of Triangular Aluminium Nanoparticles. *J. Phys. Chem. C* **2008**, *112*, 13958–13963.
70. Bi, Y.; Lu, G. Morphological Controlled Synthesis and Catalytic Activities of Gold Nanocrystals. *Mater. Lett.* **2008**, *62*, 2696–2699.
71. Kundu, S.; Lau, S.; Liang, H. Shape-Controlled Catalysis by Cetyltrimethylammonium Bromide Terminated Gold Nanospheres, Nanorods, and Nanoprisms. *J. Phys. Chem. C* **2009**, *113*, 5150–5156.
72. Li, W.; Ma, H.; Zhang, J.; Liu, X.; Feng, X. Fabrication of Gold Nanoprism Thin Films and Their Applications in Designing High Activity Electrocatalysts. *J. Phys. Chem. C* **2009**, *113*, 1738–1745.
73. Mieszawska, A. J.; Jalilian, R.; Sumanasekera, G. U.; Zamborini, F. P. Synthesis of Gold Nanorod/Single-Wall Carbon Nanotube Heterojunctions Directly on Surfaces. *J. Am. Chem. Soc.* **2005**, *127*, 10822–10823.
74. Mieszawska, A. J.; Jalilian, R.; Sumanasekera, G. U.; Zamborini, F. P. The Synthesis and Fabrication of One-Dimensional Nanoscale Heterojunctions. *Small* **2007**, *3*, 722–756.
75. Mieszawska, A. J.; Zamborini, F. P. Gold Nanorods Grown Directly on Surfaces from Microscale Patterns of Gold Seeds. *Chem. Mater.* **2005**, *17*, 3415–3420.
76. Wei, Z.; Mieszawska, A. J.; Zamborini, F. P. Synthesis and Manipulation of High Aspect Ratio Gold Nanorods Grown Directly on Surfaces. *Langmuir* **2004**, *20*, 4322–4326.
77. Wei, Z.; Zamborini, F. P. Directly Monitoring the Growth of Gold Nanoparticle Seeds into Gold Nanorods. *Langmuir* **2004**, *20*, 11301–11304.
78. Jana, N. R.; Gearheart, L.; Murphy, C. J. Wet Chemical Synthesis of High Aspect Ratio Cylindrical Gold Nanorods. *J. Phys. Chem. B* **2001**, *105*, 4065–4067.
79. Smith, D. K.; Korgel, B. A. The Importance of the CTAB Surfactant on the Colloidal Seed-Mediated Synthesis of Gold Nanorods. *Langmuir* **2008**, *24*, 644–649.
80. McFarland, A. D.; Van Duyne, R. P. Single Silver Nanoparticles as Real-Time Optical Sensors with Zeptomole Sensitivity. *Nano Lett.* **2003**, *3*, 1057–1062.
81. Murray, W. A.; Auguie, B.; Barnes, W. L. Sensitivity of Localized Surface Plasmon Resonances to Bulk and Local Changes in the Optical Environment. *J. Phys. Chem. C* **2009**, *113*, 5120–5125.
82. Slawinski, G. W.; Zamborini, F. P. Synthesis and Alignment of Silver Nanorods and Nanowires and the Formation of Pt, Pd, and Core/Shell Structures by Galvanic Exchange Directly on Surfaces. *Langmuir* **2007**, *23*, 10357–10365.
83. Lee, K.-S.; El-Sayed, M. A. Gold and Silver Nanoparticles in Sensing and Imaging: Sensitivity of Plasmon Response to Size, Shape, and Metal Composition. *J. Phys. Chem. B* **2006**, *110*, 19220–19225.
84. Miller, M. M.; Lazarides, A. A. Sensitivity of Metal Nanoparticle Surface Plasmon Resonance to the Dielectric Environment. *J. Phys. Chem. B* **2005**, *109*, 21556–21565.
85. Novo, C.; Funston, A. M.; Mulvaney, P. Direct Observation of Chemical Reactions on Single Gold Nanocrystals Using Surface Plasmon Spectroscopy. *Nat. Nanotechnol.* **2008**, *3*, 598–602.
86. Haes, A. J.; Van Duyne, R. P. A Nanoscale Optical Biosensor: Sensitivity and Selectivity of an Approach Based on the Localized Surface Plasmon Resonance Spectroscopy of Triangular Silver Nanoparticles. *J. Am. Chem. Soc.* **2002**, *124*, 10596–10604.